

Diffusion coefficients and particle transport in synthetic membrane channels

S. Pagliara^{1,2,a}, S.L. Dettmer³, K. Misiunas¹, L. Lea¹, Y. Tan¹, and U.F. Keyser¹

¹ Cavendish Laboratory, CB30HE Cambridge, UK

² Department of Biosciences, College of Life and Environmental Sciences, University of Exeter, Exeter, UK

³ Institute for Theoretical Physics – University of Cologne, Zùlpicher Str. 77, 50937 Cologne, Germany

Received 17 October 2014 / Received in final form 5 November 2014
Published online 15 December 2014

Abstract. Diffusion in constrained geometries is paramount to transport across biological membranes and in mesoporous materials. Although the transported species vary from system to system, the underlying physical mechanisms are universal. However, there is an imbalance between theory and quantitative experimental model systems. We have recently introduced a new synthetic approach to mimic molecular diffusion based on colloidal particles, digital video microscopy, particle tracking, microfluidics and holographic optical tweezers. In this paper we report useful guidelines for the fabrication, handling and characterisation of the microfluidic chips and a study of diffusion coefficients, particle attempt and translocation rates through microfluidic channels with cross sections of different dimensions.

1 Introduction

The exchange of particles and molecules across porous membranes is ubiquitous in living and synthetic systems [1–3]. In the former case particles and molecules diffuse in three dimensions in compartmentalized environments. However, particles are strongly confined and often forced into single file diffusion through membrane transport proteins that connect the different compartments [4]. The Transporter Classification Database (TCDB, approved by the International Union of Biochemistry and Molecular Biology) contains more than 10,000 non-redundant membrane transport proteins [5,6] demonstrating the wide-spread appearance of trans-membrane transport in biology. The TCDB details a comprehensive classification system for membrane transport proteins based on both functional and phylogenetic information. Transport systems are organized in five transporter classes: (i) transmembrane aqueous channels/pores like α -type channels, β -barrel porins and pore-forming toxins that catalyze movement of solutes via an energy-independent process [7]; (ii) electrochemical potential-driven transporters that utilize a carrier-mediated process to catalyze uniport, antiport and/or symport transport [8]; (iii) primary active transporters that

^a e-mail: sp608@cam.ac.uk

use a primary source of energy (chemical, electrical or solar) to drive active transport of a solute against a concentration gradient [9]; (iv) group translocators that modify the transported substrate during the transport process [10]; (v) transmembrane electron carriers that catalyze electron flow across biological membranes, from donors localized to one side of the membrane to acceptors localized on the other side [11].

On the other hand, diffusion of molecules in mesoporous materials, such as zeolites, is crucial for an ample range of applications such as mass transfer and storage, molecular sensing and catalytic conversion [12–16]. An essential requirement for the efficiency of these nano systems is that the performance is not excessively impeded by a finite rate of mass exchange between the pore volume and the surrounding compartments [17]. Recently, diffusion through more exotic materials is gaining interest; most prominently: nanotube and graphene based materials for superior transport rates [18–20] as well as solid state and DNA origami nanopores for next-generation single-molecule sensing [21,22].

2 Experimental model system: Colloidal particles, microfluidics and optical tweezers

Although an astounding number of molecular diffusion studies have been carried out both on biological and synthetic nano systems in the past 20 years [23–27], many transport mechanisms remain poorly understood due to a lack of accessibility to the channels and the fast dynamics of the transport processes (down to nanoseconds). Both theoretical [4,28–31] and experimental model systems [32–37] are essential to understand and rationalise molecular diffusion in such nano systems.

In our synthetic approach we use colloidal particles, microfluidics and holographic optical tweezers as versatile building blocks to mimic molecular diffusion in confined geometries at the sub-micron scale. Colloids are extensively used as model systems for molecules/atoms to better understand the underlying physical mechanisms of processes down to the atomic level [38–43]. Microfluidics is the emerging technology for single-molecule, particle and live cell measurements in a fully controllable microenvironment [44–50]. Holographic optical tweezers (HOTs) allow for the independent and simultaneous manipulation of multiple particles and for the generation of complex attractive energy landscapes [51–56].

We use polystyrene spherical particles to mimic the transported species, microfluidics to mimic the 3D-1D-3D complex biological environments and HOTs to generate binding sites for the particles in the microfluidic channels (Fig. 1). Taking advantage of the full control over all the parameters in the experiments we have recently investigated the diffusion of 500 nm diameter colloidal particles in 1 μm -wide channels and demonstrated some novel features of diffusion in confined geometries. Specifically, (i) we evaluated the local diffusion coefficients (in the direction perpendicular and parallel to the channel axes) from a linear fit to the local mean squared displacement (MSD)-versus-time curves [57] and found that while the perpendicular diffusion coefficient close to the confining walls decreases down to approximately 25% of the value on the channel axis, the parallel diffusion coefficient remains constant throughout the entire channel width [57]. (ii) We found that the presence of binding sites for the particles in the channel interior -generated by laser line traps- increases the particle lifetime in the channel and the translocation probability through the channel. As a consequence the translocation rate can be enhanced with an optimized potential [55], confirming the validity of previously reported theoretical models [58–62]. (iii) We demonstrated that binding sites extending from the channel interior to the surrounding 3D environments play an important role in the diffusion through the channel: they capture particles freely diffusing in the baths and allow for an enhancement in

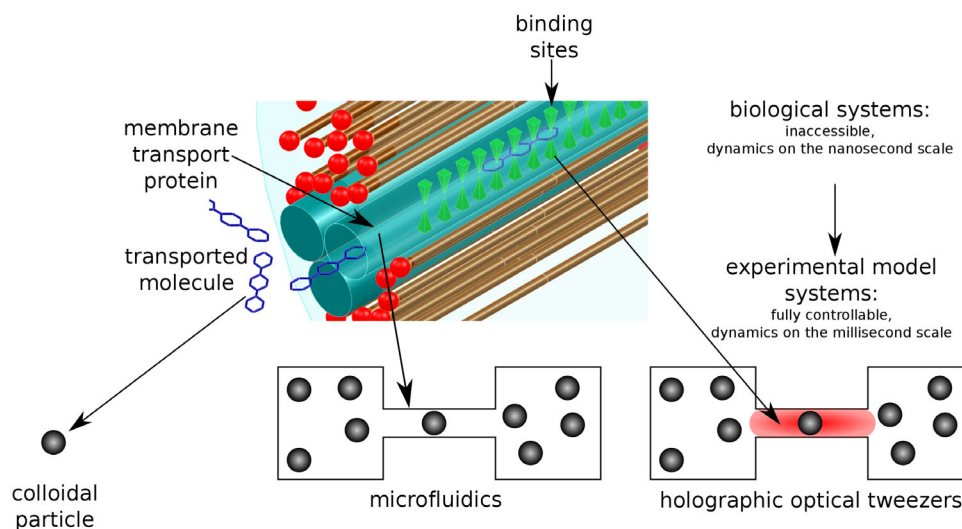


Fig. 1. Understanding membrane transport with our experimental model systems. Top: cartoon depicting molecules diffusing through a trimeric protein pore which exhibits specific binding sites for the transported molecule. Bottom: cartoon depicting our experimental model system based on colloidal particles, microfluidics and holographic optical tweezers mimicking transported molecules, membrane transport proteins and binding sites for the molecule in the protein cavity, respectively.

the rate of particles translocating the channel up to 40 times with respect to free diffusion [56].

In the following we present useful guidelines for the patterning of molds with platinum micro-wires and polymer micro-chambers (Sect. 3 and Figs. 2a–b) and of the microfluidic devices for the diffusion experiments (Sect. 4 and Figs. 2c–d). Then we illustrate our procedure to automate the experiments (Sect. 5) and we report our findings on the mechanical stress on the micro-structures in the microfluidic chip and their mechanical relaxation within the first 12 hours of the experiment (Sect. 6). Afterwards, we present our methods to assess equilibrium in the microfluidic chip (Sect. 7). Finally, we report our findings on the dependence of the diffusion properties with respect to the dimensions of the microfluidic channel cross section (Sect. 8).

3 Fabrication of the mold

The mold is fabricated in two steps: firstly, platinum micro-wires are fabricated on a silicon substrate via focused ion beam (FIB) assisted deposition (Fig. 2a); secondly, polymer micro-chambers are fabricated by photolithography (Fig. 2b).

The FIB assisted deposition of the platinum wires is carried out with a Cross-beam 1540 FIB/SEM system (Zeiss, Oberkochen, Germany) equipped with a Gemini column and a Ga^+ beam. Electron and ion beams are focused on the same point of the sample. This allows real-time simultaneous FIB machining and non-destructive scanning electron microscopy (SEM) imaging. Both imaging techniques, using a scanning electron beam or an ion beam, are possible. In our system, the electron and ion beams impinge on the sample at 90° and 36° with respect to the sample plane. Therefore during micro-machining with the ion beam the silicon sample is tilted by 54° with respect to the horizontal plane so that the ion beam perpendicularly impinges on it. The ion beam decomposes a layer of an organometallic precursor,

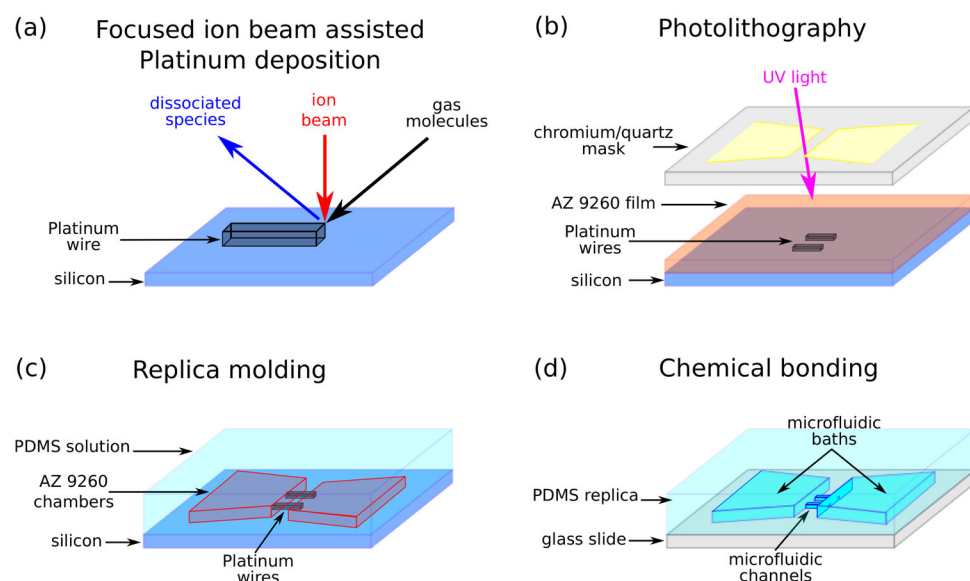


Fig. 2. Fabrication of the microfluidic chips. (a) Platinum wires are fabricated on a silicon substrate by focused ion beam assisted platinum deposition: an organometallic precursor, injected in the deposition chamber through a nozzle, is decomposed by the ion beam, this resulting in platinum atoms being deposited, and the organic fragments being exhausted from the system. (b) A $16\ \mu\text{m}$ -thick layer of AZ 9260 is spun over the wires and substrate and patterned by photolithography through a Chromium/quartz mask: the regions of the AZ layer exposed to UV light, transmitted through the Chromium-free regions of the mask, remain on the substrate after chemical development, whereas the unexposed regions on the AZ layer, under the Chromium patterns on the mask, are washed away during development. This completes the fabrication of the mold which consists of the silicon substrate, the platinum wires and the AZ micro-chambers. (c) Replica moulding from the mold to PDMS: a 9:1 (base:curing agent) PDMS mixture is poured onto the mold and cured at $70\ ^\circ\text{C}$ for 70 min in an oven. The PDMS replica is then peeled off from the mold. (d) The PDMS replica and a glass slide are exposed to an air plasma; the patterned surface of the PDMS replica is brought in contact with the glass slide and a chemical bonding is formed favoured by the air plasma functionalization of the two surfaces. The hollow structures on the PDMS surface and the glass surface form the microfluidic baths and the microfluidic channels, negative replica of the AZ micro-chambers and platinum wires, respectively.

trimethyl-methylcyclopentadienyl-platinum ($\text{C}_9\text{H}_{16}\text{Pt}$) absorbed on the sample. This dissociation results in a platinum atom being deposited, and the organic fragments diffusing away and being exhausted from the system (Fig. 2a).

The precursor crucible temperature, governing the precursor flux to the deposition area [63], is adjusted to $73\ ^\circ\text{C}$ according to the manufacturer specifications. We find it crucial to wait for at least one hour for the temperature in the crucible to stabilise before starting deposition. Depositing during the first hour typically leads to low reproducibility in the structure geometry, possibly due to temperature fluctuations in the crucible. The nozzle of the gas injection system is typically positioned at a distance $x = 16\ \mu\text{m}$, $y = 3\ \mu\text{m}$ and $z = 20\ \mu\text{m}$ from the center of the deposition area, where x and y are the coordinates on the plane of the deposition surface while z is the off-plane coordinate.

Our typical platinum deposition is carried out by using an accelerating voltage of 30 kV and a beam current of 100 pA. Higher voltages and currents lead to poor

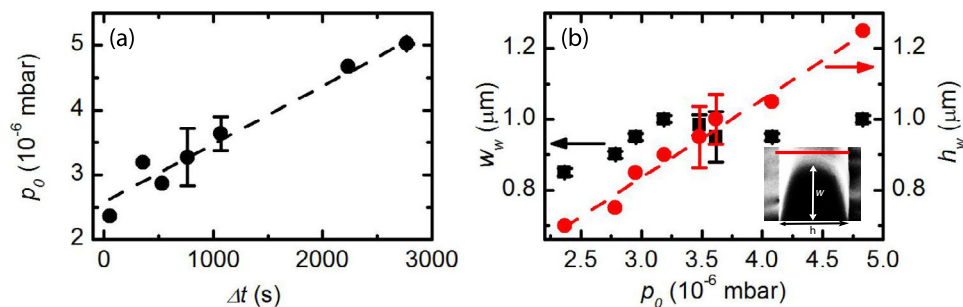


Fig. 3. Optimization of the structure fabrication via Focused Ion Beam assisted platinum deposition. (a) Dependence of the initial pressure in the chamber, p_0 , at the starting time of deposition, t_0 , on the waiting time between consecutive depositions, Δt . Error bars are the standard deviation of different pressure values measured for similar waiting time values. The dashed line is a linear fit to the data. (b) Dependence of the width, w_w , (squares, left axis) and height, h_w , (circles, right axis) of the deposited structures on p_0 . Error bars are the standard deviation of different width or height values measured for similar p_0 values (within 0.5×10^{-6} mbar). The dashed line is a linear fit to the data for h_w . Inset: typical cross section of a platinum wire as imaged with the electron beam impinging at 27° with respect to the sample plane. Scale bar: $1 \mu\text{m}$.

uniformity along the wire length and low reproducibility while lower voltages and currents required long fabrication times (tens of minutes per wire). The scanning frequencies of the ion beam are 20,000 and 0.4 Hz along the longitudinal and orthogonal wire axis, respectively, according to the manufacturer specifications.

Our goals are to deposit (i) arrays of platinum wires all with the same height and width to be used as multiple channels in which to test energy landscapes in the final device (see below) thus allowing collection of large statistics in reduced times; (ii) arrays of platinum wires with different height and width to test the effect of the channel geometry on the particle transport in the final device (see below). This requires optimising the deposition process in order to achieve good reproducibility standards. We find that a crucial parameter is the pressure in the sample chamber at the beginning of the deposition, p_0 , which is in turn related to the waiting time, Δt , between successive wire depositions. We find that p_0 scales linearly with Δt with a slope of $(9 \pm 1) \times 10^{-10}$ mbar/s and an intercept of $(2.6 \pm 0.1) \times 10^{-6}$ mbar (Fig. 3a). Such dependence is found consistently for platinum depositions on different samples and on different days. Therefore in our experiments we use Δt to control p_0 and platinum deposition.

We keep constant both the process parameters mentioned above and the requested FIB nominal wire dimensions (width $w_n = 0.6 \mu\text{m}$, height $h_n = 0.9 \mu\text{m}$ and length $l_n = 20 \mu\text{m}$) while using Δt as the only controlling parameter for platinum deposition. We image both the top view and the cross section of the wires *in situ*. In order to image each wire cross section we first use the ion beam to mill away a $1.5 \times 1.5 \mu\text{m}^2$ area of each wire tip and the surrounding silicon surface. We then tilt the sample at 27° with respect to the electron beam, and produce high magnification SEM images of the cross section of each wire (inset in Fig. 3b). We observe that Δt has little effect on the wire length, l_w which stays constant at the requested value $l_n = 20 \mu\text{m}$. Similarly the wire width, w_w , fluctuates around $0.9 \mu\text{m}$, thus 1.5 times larger with respect to w_n , without a strong dependence on p_0 (squares in Fig. 3b). On the contrary the height of the wire, h_w , depends linearly on p_0 (circles in Fig. 3b) being close to h_n for $p_0 \approx 2.5 \times 10^{-6}$ mbar. The linear fit provides a slope of $(2.2 \pm 1.1) \times 10^5 \mu\text{m}/\text{mbar}$ and an intercept of $(0.15 \pm 0.05) \mu\text{m}$. Consistent dependence is found in depositions

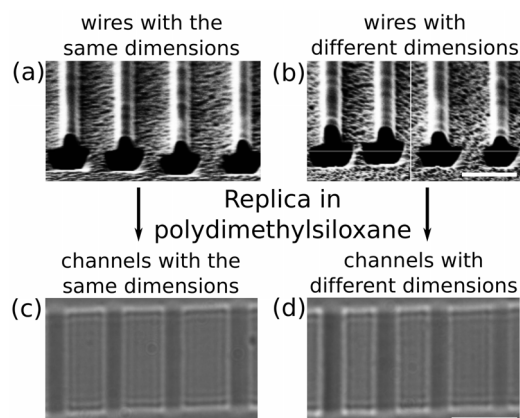


Fig. 4. Structure replica in PDMS. Arrays of platinum wires with the same (a) and different cross sections (b) produce arrays of channels with the same (c) and different cross sections (d) connecting two baths otherwise separated by a $5\ \mu\text{m}$ -long PDMS barrier. The dimensions of the platinum wires in (a) and (b) are reported in Tables 1 and 2, respectively. The angle between the direction longitudinal to the channel axes and the lateral edges of the PDMS barrier is 89° , confirming the good registration accuracy during the photolithography step discussed in Sect. 3. Scale bars: 3 micron.

on different samples and in different days allowing us to use Δt as the only parameter to control the wire height. Additionally, we adjust both Δt and w_n to obtain arrays of wires with different height and width. We reproducibly obtain arrays of wires with similar (Fig. 4a) and different dimensions (Fig. 4b). We also fabricate reference features next to each wire array to be used for autofocusing during the diffusion experiment (Sect. 5). To do so we first deposit platinum wires $1.5\ \mu\text{m}$ both in width and height next to each array of wires. Then we use the ion beam to mill away from each wire an array of squares $1.5\ \mu\text{m}$ in side with a spacing of $1.5\ \mu\text{m}$. In this way we produce an array of platinum cubes $1.5\ \mu\text{m}$ in side and spaced by $1.5\ \mu\text{m}$.

The mold is completed with the fabrication of the micro-chambers (Fig. 2b) as previously reported [64]. Briefly, a $16\ \mu\text{m}$ thick layer of AZ 9260 is patterned by conventional photolithography through a quartz mask (Photodata Ltd, Hitchin, UK) selectively coated with a thin Chromium film patterned with two symmetrical stirrup shapes separated by a $5\ \mu\text{m}$ gap and connected by two lateral channels with width and thickness of 100 and $16\ \mu\text{m}$, respectively, to facilitate hydrostatic pressure equilibration between the two reservoirs in the final microfluidic chip. The two symmetrical stirrup shapes end with four $1\ \text{mm}$ -side square pads for fluidic access in the final device. Sample and mask are carefully aligned through a MJB4 mask aligner equipped with a $5\times$ magnification objective (Karl Suss, Garching, Germany) in a way that the central region of the wire array is positioned under the $5\ \mu\text{m}$ -gap on the mask. This allows for a good registration accuracy so that the angle between the longitudinal axes of the wires and the horizontal edges of the gap on the mask is close to 90° . Importantly, the sample is baked at 60°C for 3 hours and left in air for 48 hours to allow complete evaporation of the solvent. In fact we found that replication of the mold during the first 48 hours leads to sticking of the PDMS to both the silicon and AZ 9260 surfaces and thus inducing damages to the mold.

4 Fabrication of the microfluidic chip

The fabrication of the microfluidic chip consists of two steps: firstly, the structures on the mold are replicated in a PDMS sample by replica moulding (Fig. 2c) and

Table 1. Dimensions of the array of wires in Fig. 4a, numbering is from left to right in the image.

Wire number	w_w (μm)	h_w (μm)
1	1.00	1.05
2	1.00	0.90
3	1.00	0.90
4	0.95	1.05

Table 2. Dimensions of the array of wires in Fig. 4b, numbering is from left to right in the image.

Wire number	w_w (μm)	h_w (μm)
5	1.00	1.25
6	0.95	1.05
7	0.90	0.95
8	0.85	0.70

the PDMS sample is provided with fluidic accesses; secondly the PDMS sample is chemically bonded to a glass slide via air plasma functionalization (Fig. 2d) and the fluidic accesses are sealed with a second glass slide after filling the chip with a suspension of spherical particles.

The replica of the mold is realized by casting on it a 9:1 (base:curing agent) PDMS mixture, which is let to settle and degas for 20 minutes and then cured at 70 °C for 70 min in an oven. The PDMS sample is then peeled off from the mold along the direction perpendicular to the channel array in order to minimise the mechanical stress along the longitudinal axes of the channels. Arrays of wires with the same dimensions produce arrays of channels with the same dimensions in the PDMS (wires 1–4 in Table 1 and Fig. 4a, channels 1-4 in Fig. 4c) whereas arrays of channels with varying width and height are produced from the corresponding wires on the mold (wires 5–8 in Table 2 and Fig. 4b, channels 5–8 in Fig. 4d). Four 1.5 mm-wide circular holes are drilled by a 1.5 mm-wide circular disposable biopsy punch (Kai Industries Co. Ltd., Seki City, Japan) in correspondence of the four square pads to enable fluidic access to the microchannels.

The PDMS sample and a glass slide are placed in the chamber of a plasma etcher (Diener, Royal Oak, 127 MI) and degassed for one hour. Afterwards, air is injected in the chamber at 25 sscm and the pressure in the chamber is left to stabilise for two minutes. Finally the sample and glass slides are exposed to the air plasma (2.5 W power, 10 seconds). Immediately after exposure, the patterned surface of the PDMS replica is brought in contact with the glass slide and a chemical bonding is formed favoured by the air plasma functionalization of the two surfaces. The hollow structures on the PDMS surface and the glass surface form the microfluidic baths and the microfluidic channels, negative replica of the AZ micro-chambers and platinum wires, respectively. A suspension of spherical particles in 5 mM KCl is prepared and sonicated for 15 minutes to break apart possible aggregates of colloidal particles. The colloidal particles used for the experiments reported in this paper have a diameter $2a = (505 \pm 8)$ nm according to the manufacturer specifications (Polysciences, Warrington, PA). We investigate different particle concentrations from 0.02 to $0.2 \mu\text{m}^{-3}$.

Approximately $2 \mu\text{l}$ of 5 mM KCl are injected in the bonded chip through a 27 gauge needle connected to a plastic syringe. Attention is paid to avoid the formation of air bubbles which would compromise the quality of the experiment. In this regard

we found it useful to position the blunt part of the needle close to the PDMS wall rather than the glass surface during injection. Afterwards, the four vertical fluidic accesses are completely filled with the colloidal suspension. The top surface of the device is finally sealed with a rectangular piece of a cover slip slightly larger than the PDMS sample.

5 Experiment automation

The microfluidic chip is mounted on a custom-made inverted microscope equipped with an oil immersion objective ($100\times$, 1.4 N.A., UPLSAPO, Olympus). Illumination is provided from above by an LED light (Thorlabs MWLED). The transmitted light is collected by the objective and reflected towards a charge coupled device (CCD) camera (The Imaging Source DMK 31BF03). The microscope is also equipped with holographic optical tweezers: an Ytterbium fiber laser (YLM-5-1064-LP, IPG Photonics) is passed through a beam expander and directed towards a phase-only spatial light modulator (SLM, LCOS X10468, Hamamatsu). The SLM is located in the Fourier domain of a $4f$ configuration of lenses [54] and the beam coupled into the oil immersion objective. Hot mirrors in front of the camera filter out the laser light reflected by the objective. Holographic optical traps for single colloidal particle manipulation and attractive energy landscape generation are controlled through the SLM by using a custom-made program based on LabVIEW (National Instruments) that implements a modified lens and grating algorithm [65]. Experiments were automated by using a custom-made program based on LabVIEW for positioning, autofocusing, particle manipulation and video acquisition. A *xyz*-Nanopositioning Piezo (P-561.3CD, Physik Instrumente, Karlsruhe, Germany) is controlled via a Digital-Multi-Channel Piezo Controller (E-725.3CD) in combination with a custom-written LabVIEW routine for autofocusing. The routine is based on a lookup table of images of a distinctive feature in the chip with high contrast, laterally as well as in depth, which is obtained as a negative replica of one of the reference platinum cubes described in Sect. 3. Before beginning the experiment, the chip is brought into the focal plane of the microscope by using the *xyz* piezo stage. Then the piezo stage is moved axially in 50 nm steps from -350 nm to $+350$ nm (with respect to the focal plane) and 10 lookup images stored per axial position. During the experiment, the routine determines the lookup image with the minimum mean difference of greyscale values to the current feature and thereby estimates the z displacement. The step size is not chosen smaller in order to avoid perturbations induced by movement of the piezo stage as much as possible. The lateral *xy* autofocusing is based on calculating the centre of mass (COM) of the feature after applying a brightness-contrast-gamma correction to the image and thresholding.

6 Microfluidic chip characterization

We find that the bonding of the PDMS on the glass produces a mechanical stress on the structures patterned on the PDMS sample surface obtained as a negative replica of the mold. Immediately after bonding and filling the PDMS barrier and the microfluidic channels are longer and narrower, respectively, with respect to the structures on the mold (Fig. 5a). These structures relax toward the values of the mold over time (Figs. 5b and c). Indeed it is well documented that soft elastomeric materials, such as organic polymers with Young's modulus lower than 9.0 MPa [66],

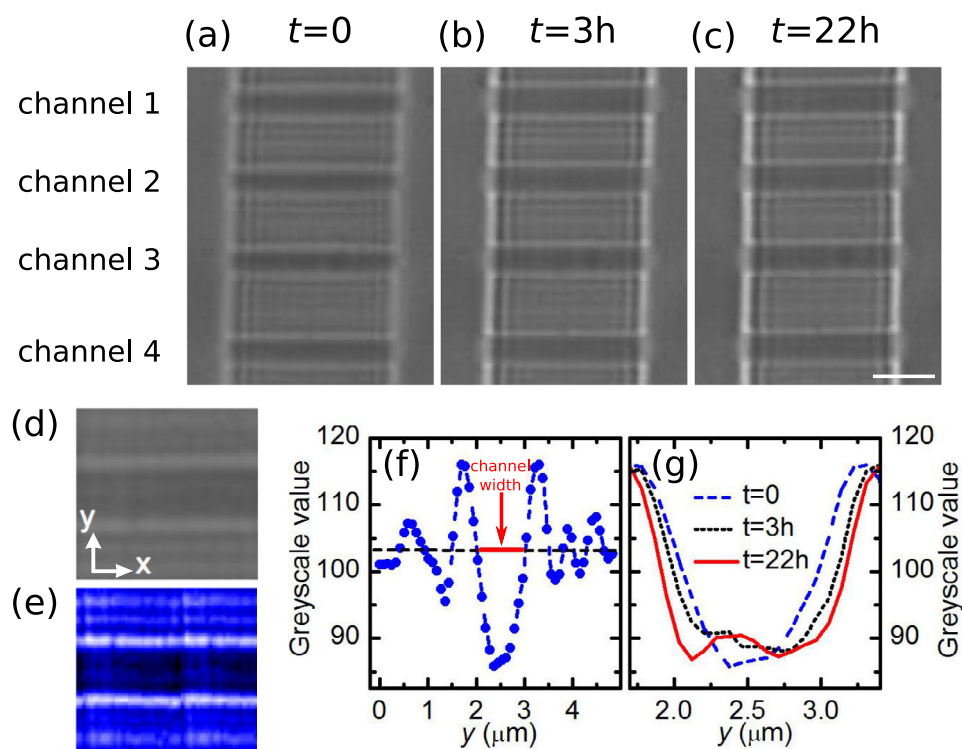


Fig. 5. Relaxation of the structures patterned on the PDMS sample after the mechanical stress imposed by the bonding on a glass slide at (a) $t = 0$ and (b) after 3 and (c) 22 hours. Scale bar: $2\ \mu\text{m}$. (d) Close up of the central section of the topmost channel at $t = 22\ \text{h}$ (e) For stronger contrast the greyscale values of the image are displayed in a color map where white indicates high light intensity and dark blue indicated low light intensity. The channel walls appear in bright white while the channel interior is darker than the rest of the image. (f) The greyscale values in the image are averaged over the x direction (image width) to give a one-dimensional light intensity profile. We utilise the fact that the channel interior is darker than the PDMS barrier and impose a threshold on the greyscale value (black dashed line) to define the channel width (red solid line). (g) Light intensity profiles for the topmost channel at $t = 0$, and after 3 and 22 hours (dashed, dotted and solid line, respectively).

are affected by pattern deformations, collapse of the structures and local sagging of the structure roof when in contact with a substrate [67,68]. However, there are no studies, to the best of our knowledge, about the relaxation in time of such soft structures after the stress induced by the strong adhesion experienced during the bonding on the substrate.

Therefore, we follow the evolution of the PDMS structures in time and in order to quantify the variation in the width of both the channels, w_c , and the PDMS barrier, w_b (corresponding to the channel length), we note that in the bright-field microscopy videos the PDMS barrier appears brighter while the microfluidic channels appear darker than the rest of the microfluidic chip in the image. Our algorithm of extracting the widths is explained in Fig. 5. First, we integrated our experimental videos of 1 h length each to give a smooth image of the channels and PDMS barrier per hour of experiment (Figs. 5a–c). For this we used 1000 images equally spaced throughout the video, i.e. 3.6 s apart, as described previously [69]. From these images we selected a small box around one channel (or a channel free section of the PDMS barrier) (Fig. 5d)

Table 3. Extension parameters derived from the exponential fit for channels 1–4 obtained as a negative replica of the platinum wires 1–4 reported in Table 1. Errors are less than 5% of the reported values.

structure	w_0 [μm]	w_f [μm]	α [h^{-1}]
channel 1	0.88	1.10	0.34
channel 2	0.87	1.01	0.36
channel 3	0.86	1.10	0.53
channel 4	0.89	1.01	0.47
PDMS barrier	5.41	4.95	0.26

and evaluated the light intensity in each pixel as the 8 bit greyscale value displayed in a color map in Fig. 5e. We calculated the one-dimensional light intensity across the channel (PDMS barrier) width by averaging over the translationally symmetric direction (Figs. 5f and g). To this intensity profile we applied a threshold to determine the width of the channel or the PDMS barrier, respectively. The intersection of the intensity profile with the threshold was calculated by linearly interpolating between the two points where the threshold is crossed which allows for subpixel resolution. Since the channel width is on the order of the wavelength of visible light, the light intensity outside of the channel is not flat but shows characteristic diffraction patterns (the white stripes in Fig. 5e and oscillations in the light intensity profile in Fig. 5f). We choose the average light intensity outside of the channel as the intensity threshold (Fig. 5f). This corresponds well with the width determination from visual inspection of the original bright field images. In order to compensate for any absolute changes in illumination during the experiment, all intensity profiles are normalized to the same maximum intensity. We estimate that our algorithm incurs an error of ~ 0.5 px ≈ 34 nm on the total width. Possible drift or fluctuations in the z position are limited by our auto-focusing routine to ~ 25 nm on average which translates into an additional error of ~ 35 nm (our numerical aperture is 1.4). By gaussian error propagation this gives a total accuracy of ~ 50 nm.

We follow the relaxation of the channel and barrier width during the first day after bonding on the glass slide and find the behaviour presented in Fig. 6. A simple model for the dependence of the channel and barrier width on the time after bonding would be that the rate of width change is proportional to its difference from some saturation value:

$$\frac{d}{dt}w(t) = -\alpha(w(t) - w_f) \quad (1)$$

where $w(t)$ is the time dependent width, w_f the saturation width, and α describes the speed of the relative linear extension.

The solution to this ODE is obviously

$$w(t) = w_f + [w(0) - w_f]e^{-\alpha t}. \quad (2)$$

The resulting fitting parameters for the channel and PDMS barrier size extension can be found in Table 3. Independent of the applied model we observe that the width of the channels approaches that of the platinum wires on the mold with increasing time while being compressed initially. We are currently investigating the relaxation of the microfluidic channels along their height but we can hypothesize a similar behaviour to the one reported along their width.

Furthermore we also measure the concentration of particles in both baths. To this end we use a custom-made LabVIEW routine that takes one hour of experimental video as input and counts the number of particles in every 100th frame (1000 frames per hour of video) by applying a common particle segmentation algorithm [57]. The

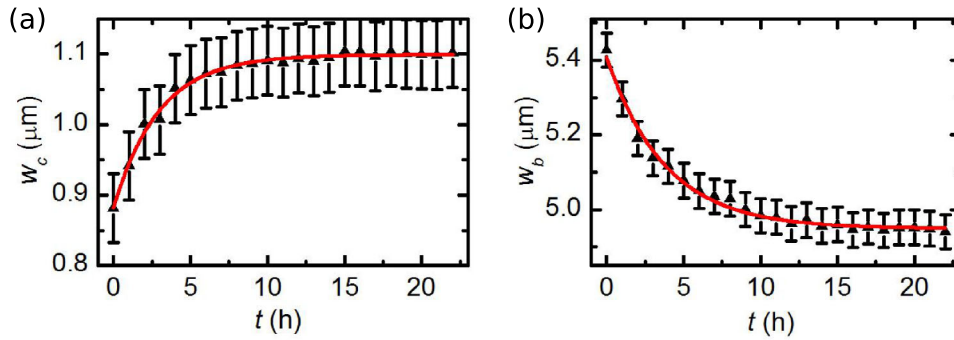


Fig. 6. Dependence of (a) channel and (b) the PDMS barrier width on the time elapsed from the bonding and filling of the microfluidic chip. The solid lines are exponential fits to the data by using Eq. (2). Values for the parameters estimated from the fit are reported in Table 3.

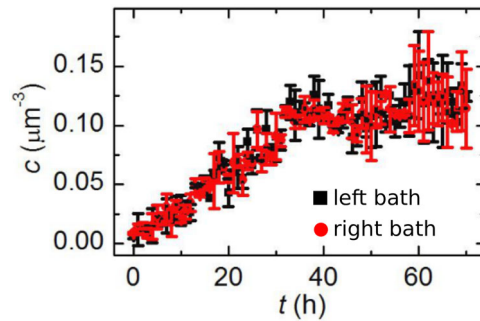


Fig. 7. Dependence of the particle concentration in the left (black squares) and right (red circles) bath on the elapsed time from the bonding and filling of the microfluidic chip.

particle concentration is determined by averaging over the analysed frames and dividing by the lateral analysed area times the approximate tracking depth which is determined from a calibration experiment. Particles that are stuck to the glass slide, i.e., they appear at the same position in two consecutive analysed frames, are discarded. Figure 7 reports the dependence of the concentration of particles in the left (black squares) and right bath (red circles) on the elapsed time after the filling of the microfluidic chip. The concentration linearly increases in both baths in the first 24 hours after filling before reaching the value expected from the bulk measurement ($0.1 \mu\text{m}^{-3}$) at which it stays up to 70 hours after filling. In fact, we minimise water loss by sealing the top surface of the device with a rectangular piece of a cover slip slightly larger than the PDMS sample. However, water is still lost (i) in the bulk PDMS along the walls of micro-channels and chambers (volumetric loss) and (ii) through the lateral walls of the bulk PDMS that are not sealed with cover slip (vapour loss) [70]. We evaluate water loss in our microfluidic devices according to the simple model presented in [70] and our measured parameters. We find a volumetric loss around $7 \mu\text{l}$ and a vapour loss around $2 \mu\text{l}$ per day. The volumetric loss occurs within the first 24 hours after filling, a period in which we typically do not carry out any particle diffusion measurements (see next paragraph) while the vapour loss is negligible with respect to the initial volume of fluid injected in the chip (around $100 \mu\text{l}$).

7 Assessment of equilibrium in the microfluidic chip

In order to assess Brownian motion of the spherical particles in the microfluidic chip we carry out control experiments both in the beginning and throughout the entire duration of the experiments. We use the acquired bright-field microscopy videos to track the particle positions at all times both in the channels and in the regions of the baths next to the channel. First individual particles are identified in each video frame (segmentation) by frequency-filtering and thresholding and then the COM position is determined at subpixel resolution from the particle greyscale values [57]. Particle positions of multiple particles in subsequent frames are linked into trajectories by a nearest neighbour algorithm that takes into account conditions imposed by the quasi-one-dimensional channels, i.e., particles cannot pass each other and particles may enter or exit the channel at the end of the channel only. Furthermore, particles at the ends of the tracked region (5 pixels in the regions of the baths in front of the channels) are discarded since the COM is falsely shifted toward the channel when only half of the particle is visible in the tracking region.

We define an attempt as the event for which a particle enters into the channel from either bath and explores it for at least 100 milliseconds. The same particle may enter and exit the channel multiple times. Once a particle has entered the channel, it can either go back to the same bath, defined as a return event, or translocate the channel and exit to the opposite bath, defined as a translocation event. We characterise the transport in terms of the attempt rate, J_a , and translocation rate, J_t .

We typically carry out our diffusion experiments around 24 hours after bonding, when (i) the PDMS structures have mechanically relaxed back to their original shape (Fig. 6), (ii) the particle concentration in the baths has reached a steady state (Fig. 7) and (iii) the baths and the microfluidic channels have reached equilibrium so that there is no preferential particle diffusion from one bath to the other. To test the last point we typically characterise free diffusion for all the channels in the microfluidic chip for at least 5 hours before starting our diffusion experiments. We first measure J_a for the microfluidic channels obtained as a negative replica of the wires introduced in Tables 1 and 2 in order to test whether the channels with similar dimensions behave similarly in free diffusion. The values reported in Fig. 8a are obtained as the average and standard deviation of the measurements in 5 different 1h-long videos. J_a is indeed similar within the error bar for channels 1–4. However, the slightly larger dimensions of channel 1 (see Table 1) allow for a higher J_a . Instead, J_a monotonously decreases from 50 to less than 1 particle per hour when comparing channels 5–8 which are purposely fabricated with decreasing dimensions (see Table 2).

We measure the difference in the number of particle attempts to enter each channel from the right and left bath, $J_{a,r-l}$. Figure 8b reports the values of $J_{a,r-l}$ for the channels, averaged over the measurements for the 5 videos. $J_{a,r-l}$ is close to zero within the error bar for the eight measured channels, confirming that there is no preferential bias from one bath to the other and thus equilibrium in the microfluidic chip. In our typical experiments for testing the effect of binding sites on particle transport, we couple laser line traps that generate attractive energy landscapes in some of the microfluidic channels while leaving at least one channel in free diffusion [56]. The constant monitoring of free diffusion is crucial for the continuous assessment of Brownian motion.

8 Dependence of diffusion properties on channel geometry

In order to further investigate the dependence of particle diffusion on the dimensions of the channel cross section we typically carry out 12 hours long experiments with all

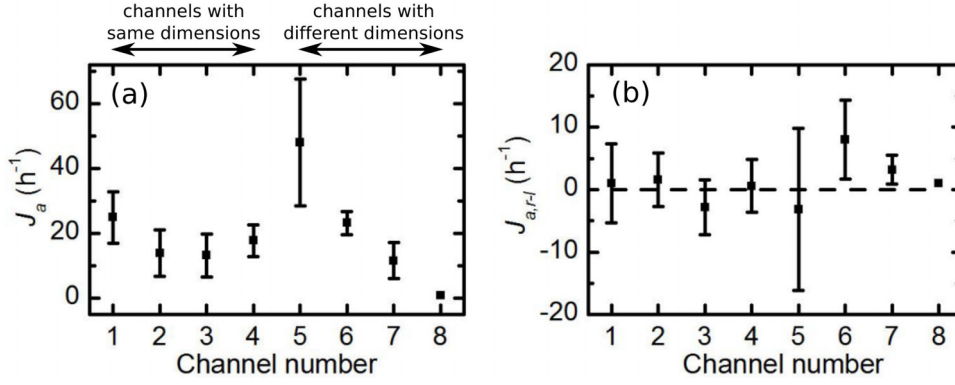


Fig. 8. Assessment of free diffusion in the microfluidic channels. (a) J_a and (b) $J_{a,r-l}$ for the 8 microfluidic channels obtained as negative replica of the wires reported in Tables 1 and 2. Each data point and corresponding error bar are the mean and standard deviation of five independent measurements lasting one hour. The dashed line indicates no net flow and thus equilibrium between the two baths.

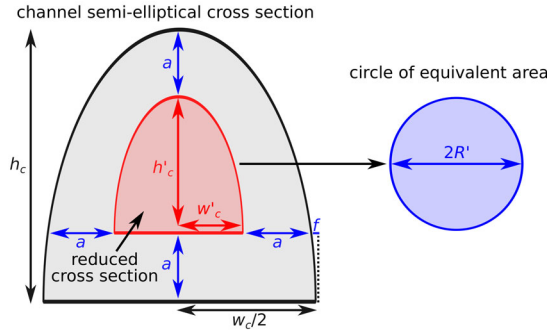


Fig. 9. The channel cross section (grey shaded area, semi-ellipse with major axis h_c and minor axis $w_c/2$) decreases to a reduced cross section (red shaded area, semi-ellipse with major axis h'_c and minor axis w'_c) taking into account the finite particle size ($2a = 505$ nm). This can be approximated by a circle of equivalent area (blue shaded area, circle of radius R).

the channels in free diffusion. We also used a high particle concentration (0.2 colloidal particles μm^{-3}) to produce a larger statistical sample of measurements.

It is noteworthy that, taking into account the finite size of the colloidal particles ($2a = 505$ nm), the half width and the height of the channel (Fig. 9) reduce to:

$$w'_c = \frac{w_c - 2a}{2} f = \frac{w_c - 2a}{2} \sqrt{1 - \left(\frac{a}{h_c - a}\right)^2} \quad (3)$$

$$h'_c = h_c - 2a. \quad (4)$$

For each channel we evaluate the radius of the circle with area equivalent to the one of the channel reduced cross section, R' (Fig. 9):

$$R' = \sqrt{\frac{w'_c h'_c}{2}} \quad (5)$$

where the factor 2 accounts for the semi-ellipse.

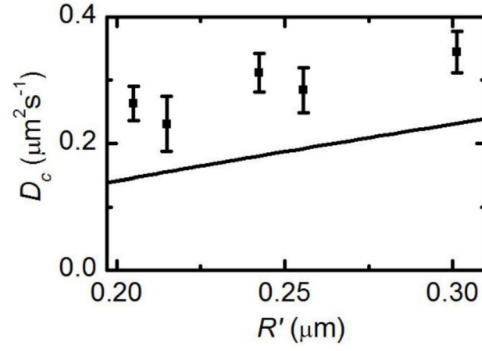


Fig. 10. Dependence of the average D_c on R' . The data and error bars for each channel are obtained as the mean and standard deviations of the diffusion coefficient measurements over all the bins in the channel. The reported measurements are for channels 7, 2, 6, 1 and 5 (in order of ascending R'). The measurements for channels 3 and 4 are close to the one for channel 2 and are omitted for clarity. The measurements on channel 8 are not statistically significant. The solid line is a prediction according to the Bungay theory with our measured parameters.

Firstly, we measure the particle diffusion coefficient in the channels, D_c , determined from a linear fit to the first two points of mean squared displacement (MSD)-versus-time curves which are extracted from the trajectories of particles exploring the channels and then averaged over all trajectories [57,69]. While analytical predictions for D_c in semi-elliptical channels are not available, Bungay and Brenner predicted the diffusion coefficient of spheres diffusing in infinitely long cylindrical channels of arbitrary radius, R' , by calculating the viscous drag force from the solution of the Stokes equation [71]. Figure 10 reports the dependence of the particle diffusion coefficient, D_c , on R' . D_c increases with R' according to the Bungay theory. The measured values are higher than predicted, possibly due to the semi-elliptical shape of the microfluidic channels.

Secondly, we measure J_a for the different microfluidic channels obtained as the average of 12 hours of experiments. J_a increases with R' (Fig. 11a), according to the dependence expected for the diffusion current through a disk-like absorber of radius R' in a semi-infinite medium (Eq. 2.21 in [72]):

$$J_a = 2(4D_b R')c \quad (6)$$

where the factor 2 takes into account both apertures of the channel to the baths, $D_b = (0.74 \pm 0.03) \mu\text{m}^2\text{s}^{-1}$ and $c = (0.21 \pm 0.02) \mu\text{m}^{-3}$ are obtained as the averages of the values in 12 different videos. It is noteworthy that D_b is actually not constant in the baths: particles approaching the channel mouths exhibit lower diffusion coefficients than the ones far away from the PDMS barrier (Fig. 2 in [57]). However, in Eq. (6) we assume D_b to be spatially constant for the sake of simplicity. A better prediction for J_a can be obtained by considering the expression for the diffusion current through an elliptical absorber in a semi-infinite medium [73]:

$$J_a = 2D_b \frac{1}{2} \sqrt[3]{\frac{32AP}{\pi}} c = D_b \sqrt[3]{\frac{32AP}{\pi}} c \quad (7)$$

where A and P are the area and perimeter of the ellipse, respectively, 2 accounts for both apertures of the channel and 1/2 for the semi-elliptical shape. Figure 11b compares the dependence of measured (squares) and predicted (line) J_a on the

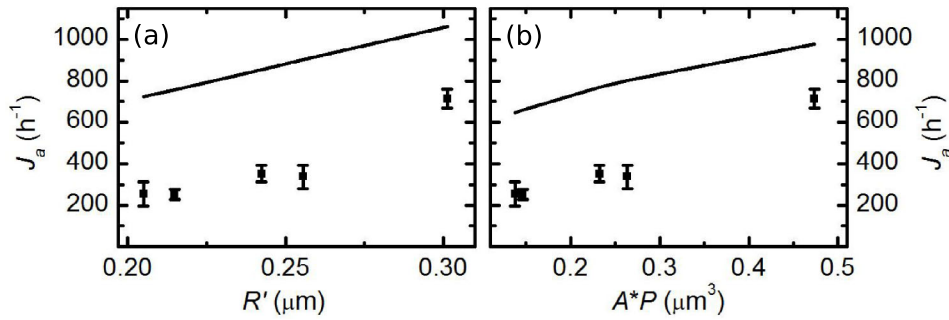


Fig. 11. Dependence of J_a on the dimensions of the channel cross section. Dependence of the measured J_a on (a) R' and (b) AP . Each data point and corresponding error bar are the mean and standard deviation of twelve independent measurements lasting one hour. The solid lines are the predicted values calculated according to Eqs. (6) and (7), respectively, with the experimental parameters determined from our measurements.

product AP . The measured J_a is smaller than predicted. This presumably stems from both our approximation of D_b as a constant and our definition of attempt as a particle that explores the channels for at least 100 ms and thus to the fact that we do not count very short events.

J_t increases with R' (Fig. 12) according to the following equation previously derived [55, 59, 74, 75]:

$$J_t = 4 \frac{4\pi D_b D_c R'^2 c}{(2\pi D_c R' + 4D_b L)(2 + R'^2 c\pi L)} \quad (8)$$

where $D_c = (0.29 \pm 0.04) \mu m^2 s^{-1}$ is the diffusion coefficient in the channels obtained as the average of the values measured for the different channels (Fig. 10). The measured data (black squares) are in good agreement with the predicted behaviour (solid line) apart from the channel with $R' > 0.3 \mu m$ where particles are not in single file diffusion and thus violate the assumptions of the theoretical model. The red circles in Fig. 12 present a better prediction for J_t calculated by using the single diffusion coefficient values measured for the different channels and reported in Fig. 10.

It is noteworthy that channel 5, being one and a half times larger in R' with respect to channel 7, allows for a 3-fold enhancement in J_t and J_a . On the other hand, we have recently demonstrated with our experimental model system that particle transport can be enhanced far stronger by using holographic optical tweezers to introduce optical traps for the transported particles both inside and outside the channel [56].

9 Conclusions

We presented and characterised an experimental model system, at the sub-micron scale, based on colloidal particles, microfluidics and holographic optical tweezers to investigate molecular diffusion through membrane transport proteins and synthetic nanopores. We optimised the fabrication of the microfluidics via focused ion beam assisted platinum deposition finding that the dimensions of the deposited structures are strongly correlated with the pressure in the deposition chamber and with the waiting time between successive depositions. This allowed us to accurately control the deposition of arrays of platinum wires with the same cross section as well as

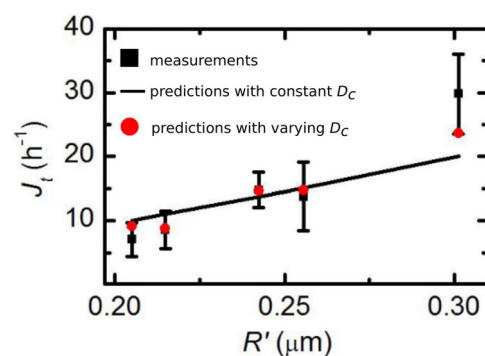


Fig. 12. Comparison of measured (black squares) and predicted J_t (solid line and red circles) as a function of R' . Each data point and corresponding error bar are the mean and standard deviation of twelve independent measurements lasting one hour. The solid line presents values calculated according to Eq. (8) with the experimental parameters determined from our measurements and by using a constant value of D_c for all channels ($D_c = 0.29 \mu\text{m}^2/\text{s}$). The red circles present the values calculated by using the values of D_c measured for each channel and reported in Fig. 10.

arrays with wires with different dimensions. We found that the negative replica of such wires replicated in PDMS is subject to an intense mechanical stress after the bonding to the glass slide. We used digital video microscopy to characterise the relaxation of such structures over time and found that these approach their original shape around twelve hours after bonding. Similarly we used digital video microscopy to quantify the particle concentration in the baths and found that this reaches the bulk value 24 hours after filling the microfluidic chip. Furthermore, we characterised particle diffusion through channels with different cross section dimensions. We found that the attempt rate increases with the radius of the circle with equivalent area to the channel semi-elliptical cross section. We compared our measurements with the predicted diffusion current for both a circular and an elliptical absorber and found for both cases that the measured attempt rate was lower than the predicted one, probably due to the fact that we approximate the diffusion coefficient of particles in the baths as constant and we do not measure attempts shorter than 100 ms. We found that also the translocation rate increases with the equivalent radius in good accordance with theoretical models for single particle diffusion through channels. Importantly, increasing the channel dimensions produced a maximum enhancement of a factor of 3 in the attempt and translocation rate, respectively. On the contrary we have recently shown that varying the energy landscape in the very same channel can produce an enhancement of up to a factor of two orders of magnitude and 40 in the attempt and translocation rate, respectively. Our findings confirm the importance of the interaction between the transporter channel and the transported species. The presented model system can be used to validate theoretical model systems of transport processes, as a powerful complementary tool to elucidate the mechanisms of diffusion through membrane transport proteins present in the Transporter Classification Database, ultimately to guide the design of both new drugs and more efficient synthetic membranes.

S.P. acknowledges the support from the Leverhulme and Newton Trust through an Early Career Fellowship. S.L.D. acknowledges funding from the German Academic Exchange

Service (DAAD) and the German National Academic Foundation. U.F.K. was supported by an ERC starting grant.

References

1. B. Alberts, A. Johnson, J. Lewis, M. Raff, K. Roberts, P. Walter, *Molecular Biology of the Cell* (Garland, 2008)
2. J.W.F. Robertson, J.J. Kasianowicz, S. Banerjee, *Chem. Rev.* **112**, 6227 (2012)
3. T. Chou, D. Lohse, *Phys. Rev. Lett.* **82**, 3552 (1999)
4. P.C. Bressloff, J.M. Newby, *Rev. Mod. Phys.* **85**, 135 (2013)
5. M.H. Saier Jr., C.V. Tran, R.D. Barabote, *Nucl. Acids Res.* **34**, D181 (2006)
6. M.H. Saier Jr., V.S. Reddy, D.G. Tamang, A. Vastermark, *Nucl. Acids Res.* **42**, D251 (2014)
7. S.W. Cowan, T. Schirmer, G. Rummel, M. Steiert, R. Ghosh, R.A. Pauptit, J.N. Jansonius, J.P. Rosenbusch, *Nature* **358**, 727 (1992)
8. L.R. Forrest, R. Krämer, C. Ziegler, *Biochim. Biophys. Acta* **1807**, 167 (2011)
9. W. Saurin, M. Hofnung, E. Dassa, *J. Mol. Evol.* **48**, 22 (1999)
10. Y.J. Reizer, M.H. Saier, Jr., W.J. Fairbrother, P.E. Wright, *Biochemistry* **32**, 32 (1993)
11. M. Geiszt, T.L. Leto, *J. Biol. Chem.* **279**, 51715 (2004)
12. F. Schüth, K.S.W. Sing, J. Weitkamp, *Handbook of Porous Solids* (Wiley-VCH, 2002)
13. F. Laeri, F. Schüth, U. Simon, M. Wark, *Host?Guest Systems Based on Porous Crystals* (Wiley-VCH, 2003)
14. S.M. Auerbach, K.A. Carrado, P.K. Dutta, *Handbook of Zeolite Science and Technology* (Taylor & Francis, 2003)
15. G. Ertl, H. Knözinger, F. Schüth, J. Weitkamp, *Handbook of Heterogeneous Catalysis* (Wiley-VCH, 2008).
16. J. Kärger, R. Valiullin, *Chem. Rev. Soc.* **42**, 4172 (2013)
17. J. Kärger, D.M. Ruthven, D. Theodorou, *Diffusion in Nanoporous Materials* (Wiley-VCH, 2012)
18. A. Siria, P. Poncharal, A.-L. Bianco, R. Fulcrand, X. Blase, S. T. Purcell, L. Bocquet, *Nature* **494**, 255 (2014)
19. R.K. Joshi, P. Carbone, F.C. Wang, V.G. Kravets, Y. Su, I.V. Grigorieva, H.A. Wu, A.K. Geim, R.R. Nair, *Science* **343**, 752 (2014)
20. Z. Yao, C.L. Kane, C. Dekker, *Phys. Rev. Lett.* **84**, 2941 (2000)
21. N.A.W. Bell, U.F. Keyser, *Febs Lett.* doi: 10.1016/j.febslet.2014.06.013 (2014)
22. S.W. Kowalczyk, C. Dekker, *Nano Lett.* **12**, 4159 (2012)
23. V. Kukla, J. Kornatowski, D. Demuth, I. Girnus, H. Pfeifer, L.V.C. Rees, S.K.K. Unger, J. Kärger, *Science* **272**, 702 (1996)
24. J. Kärger, T. Binder, C. Chmelik, F. Hibbe, H. Krautscheid, R. Krishna, J. Weitkamp, *Nat. Mater.* **13**, 333 (2014)
25. E.M. Nestorovich, C. Danelon, M. Winterhalter, S.M. Bezrukov, *Proc. Nat. Acad. Sci.* **99**, 9789 (2002)
26. C. Hilty, M. Winterhalter, *Phys. Rev. Lett.* **86**, 5624 (2001)
27. R.M.M. Smeets, U.F. Keyser, D. Krapf, M.Y. Wu, N.H. Dekker, C. Dekker, *Nano Lett.* **6**, 89 (2006)
28. P.S. Burada, P. Hänggi, F. Marchesoni, G. Schmid, P. Talkner, *Chem. Phys. Chem.* **10**, 45 (2009)
29. P. Hänggi, F. Marchesoni, *Rev. Mod. Phys.* **81**, 387 (2009)
30. S. Redner, *A guide to first-passage processes* (Cambridge University Press, 2001)
31. M. Muthukumar, *Polymer translocation* (CRC Press, 2011)
32. Q.H. Wei, C. Bechinger, P. Leiderer, *Science* **287**, 625 (2000)
33. Y. Caspi, D. Zbaida, H. Cohen, M. Elbaum, *Nano Lett.* **11**, 3728 (2008)
34. S.W. Kowalczyk, L. Kapinos, T.R. Blosser, T. Magalhães, P. van Nies, R.Y.H. Lim, C. Dekker, *Nat. Nanotechnol.* **6**, 433 (2011)

35. Y. Wang, Y. Wang, D.R. Breed, V.N. Manoharan, L. Feng, A.D. Hollingsworth, M. Weck, D.J. Pine, *Nature* **491**, 51 (2012)
36. K.D. Schleicher, S.L. Dettmer, L.E. Kapinos, S. Pagliara, U.F. Keyser, S. Jeney, R.Y.H. Lim, *Nat. Nanotechnol.* **9**, 525 (2014)
37. B. Lin, M. Meron, B. Cui, S.A. Rice, *Phys. Rev. Lett.* **94**, 216001 (2005)
38. V.J. Anderson, H.N.W. Lekkerkerker, *Nature* **416**, 811 (2002)
39. U. Gasser, E.R. Weeks, A. Schofield, P.N. Pusey, D.A. Weitz, *Science* **292**, 258 (2001)
40. H. Wang, T.-S. Chung, Y.W. Tong, K. Jeyaseelan, A. Armugam, Z. Chen, M. Hong, W. Meier, *Small* **8**, 1185 (2012)
41. R.J. Macfarlane, B. Lee, M.R. Jones, N. Harris, G.C. Schatz, C.A. Mirkin, *Science* **334**, 204 (2011)
42. L. Di Michele, E. Eiser, *Phys. Chem. Chem. Phys.* **15**, 3115 (2013)
43. L. Di Michele, F. Varrato, J. Kotar, S.H. Nathan, G. Foffi, E. Eiser, *Nature Comm.* **4**, 2007 (2013)
44. D. Psaltis, S.R. Quake, C.H. Yang, *Nature* **442**, 381 (2006)
45. L. Mazutis, J. Gilbert, W.L. Ung, D.A. Weitz, A.D. Griffiths, J.A. Heyman, *Nat. Protoc.* **8**, 870 (2013)
46. S. Pagliara, C. Chimere, R. Langford, D.G.A.L. Aarts, U.F. Keyser, *Lab Chip* **11**, 3365 (2011)
47. S. Pagliara, K. Franze, C.R. McClain, G.W. Wylde, C.L. Fisher, R.J.M. Franklin, A.J. Kabla, U.F. Keyser, K.J. Chalut, *Nat. Mater.* **13**, 638 (2014)
48. D.R. Gossett, H.T.K. Tse, A.L. Lee, Y. Ying, A.G. Lindgren, O.O. Yang, J. Rao, A.T. Clark, D. Di Carlo, *Proc. Natl. Acad. Sci. USA* **109**, 7630 (2012)
49. A.E. Ekpenyong, G. Whyte, K. Chalut, S. Pagliara, F. Lautenschläger, C. Fiddler, S. Paschke, U.F. Keyser, E.R. Chilvers, J. Guck, *PLoS One* **7**, e45237 (2012)
50. S. Kim, A.M. Streets, R.R. Lin, S.R. Quake, S. Weiss, D.S. Majumdar, *Nat. Methods* **8**, 242 (2011)
51. J.E. Curtis, B.A. Koss, D.G. Grier, *Opt. Commun.* **207**, 169 (2002)
52. D. Grier, *Nature* **424**, 810 (2003)
53. M. Padgett, R. Bowman, *Nat. Photonics* **5**, 343 (2011)
54. M. Padgett, R. Di Leonardo, *Lab Chip* **11**, 1196 (2011)
55. S. Pagliara, C. Schwall, U.F. Keyser, *Adv. Mater.* **25**, 844 (2014)
56. S. Pagliara, S.L. Dettmer, U.F. Keyser, *Phys. Rev. Lett.* **113**, 048102 (2014)
57. S.L. Dettmer, S. Pagliara, K. Misiunas, U.F. Keyser, *Phys. Rev. E* **89**, 062305 (2014)
58. A.M. Berezhkovskii, S.M. Bezrukov, *Chem. Phys.* **319**, 342 (2005)
59. A.M. Berezhkovskii, S.M. Bezrukov, *Biophys. J.* **88**, L17 (2005)
60. A.B. Kolomeisky, *Phys. Rev. Lett.* **98**, 048105 (2007)
61. W.R. Bauer, W. Nadler, *Proc. Natl. Acad. Sci. USA* **103**, 11446 (2006)
62. A. Zilman, *Biophys. J.* **96**, 1235 (2009)
63. K.A. Telari, B.R. Rogers, H. Fang, L. Shen, R.A. Weller, D.N. Braski, *J. Vac. Sci. Technol. B* **20**, 590 (2002)
64. S. Pagliara, C. Chimere, D.G.A.L. Aarts, R. Langford, U.F. Keyser, *Prog. Coll. Pol. Sci.* **139**, 45 (2012)
65. R. Bowman, V. D'Ambrosio, E. Rubino, O. Jedrkiewicz, P. Di Trapani, M.J. Padgett, *Eur. Phys. J. Special Topics* **199**, 149 (2011)
66. A. Bietsch, B. Michel, *J. Appl. Phys.* **88**, 4310 (2000)
67. J. Hu, R.G. Beck, T. Deng, R.M. Westervelt, K.D. Maranowski, A.C. Gossard, G.M. Whitesides, *Appl. Phys. Lett.* **71**, 2020 (1997)
68. S. Pagliara, L. Persano, A. Camposeo, R. Cingolani, D. Pisignano, *Nanotechnology* **18**, 175302 (2007)
69. S.L. Dettmer, U.F. Keyser, S. Pagliara, *Rev. Sci. Instrum.* **85**, 023708 (2014)
70. A.R. Prakash, S. Adamia, V. Sieben, P. Pilarski, L.M. Pilarski, C.J. Backhouse, *Sensor. Actuat. B-Chem.* **113**, 398 (2006)
71. P. Bungay, H. Brenner, *Int. J. Multiphase Flow* **1**, 25 (1973)
72. H.C. Berg, *Random walks in biology* (Princeton University Press, 1993)

73. O. Dudko, A. Berezhkovskii, G. Weiss, *J. Chem. Phys.* **121**, 1562 (2004)
74. A.M. Berezhkovskii, M.A. Pustovoit, S.M. Bezrukov, *J. Chem. Phys.* **116**, 9952 (2002)
75. A.M. Berezhkovskii, M.A. Pustovoit, S.M. Bezrukov, *J. Chem. Phys.* **119**, 3943 (2003)
76. R. Dutzler, Y.F. Wang, P.J. Rizkallah, J.P. Rosenbusch, T. Schirmer, *Structure* **4**, 127 (1996)